Article

Galaxy Number Counts from the Sloan Digital Sky Survey

John H. Marr [1,†,‡]

[1] john.marr@2from.com
Unit of Computational Science
Building 250, Babraham Research Campus, Cambridge
CB22 3AT, UK

Abstract: Data from DR17 of the SDSS in the g, i, r, u, z bands were used to compute galaxy number counts and galaxy density per square degree in the composite b_J band over two areas of sky centred on the North Galactic Cap (NGC) and above the South Galactic Cap (SGC), with areas of 5,954 and 859 sq. deg. respectively and a combined count of 622,121 galaxies within the limits of redshift ≤ 0.4 and $b_J \leq 20$. The comparative densities confirmed an extensive void in the Southern sky with a deficit of 26% out to a redshift $z \sim 0.15$. Number counts in the $K-$, $R-$, $I-$, $H-$, $B-$ and $U-$bands were derived from the Durham Extragalactic Astronomy and Cosmology catalogue and were well fitted to a general relativity (GR) cosmological model over their whole range, requiring only modest luminosity evolution, except for a steeper curve in the $B-$band at faint magnitudes required a star-burst evolutionary model to account for the excess faint number counts. Extending the SDSS redshift-number count survey to fainter and more distant galaxies with redshift ≤ 1.20 and $b_J \leq 24$ showed a secondary peak in the number counts that may account for this observed apparent excess of faint blue galaxy counts. Individual examination of a sample of these galaxies suggested that many were QSOs, bright X-ray or radio sources, or evolving irregular galaxies with rapid star formation rates. This sub-population at redshifts $0.45 - 0.65$ may account for the excess counts observed in the $B-$ optical band.

Keywords: galaxies: number counts; general relativity; dark matter; dark energy

1. Introduction

The mean number of galaxies/unit volume of space is conceptually straightforward, with the potential to provide deeper probes than methods that rely on purely spectroscopic observations. Galaxies are counted in a specified colour band across a fixed area of sky, and binned into apparent magnitude or half magnitude bins. One large source of error is that each bin contains galaxies with a range of morphologies and redshifts, and hence age and evolutionary history, so individual bins may require a range of corrections which have to be averaged for each bin. Attempts have been made to clarify these averaged counts by attempting to bin by morphology and redshift, but this defeats the essential simplicity of complete magnitude counts. Despite these limitations, galaxy number counts provide one of the most straightforward measurable quantities in cosmology. The faint magnitude depth has been regularly extended over the years for each spectral band, and many individual series of observations have been collated and published by the Extragalactic Astronomy and Cosmology Research Group of Durham University [1]. Initial data is drawn from the Sloane Digital Sky Survey (SDSS), which has provided increasing quantities of data since their first data release in 2003 until their most recent data release of DR17, which became publicly available in December 2021 [2], with detailed information on large number of galaxies across five colour bands out to apparent magnitude limits of $\sim 21 - 23$.

2. Data from the SDSS

The most recent update to the SDSS is DR17 which became publicly available in December 2021 [2] and has provided a wealth of data over five spectral colours, with spectra and usable redshifts for ~ 2.6 million unique galaxies out to limiting magnitudes of u'=22.3, g'=23.3, r'=23.1, i'=22.3, and z'=20.8. Two principle areas were considered from the

Citation: Marr, J.H. Galaxy Number Counts from the SDSS. *Preprints* **2022**, *1*, 0. https://doi.org/

Preprints (www.preprints.org) | NOT PEER-REVIEWED | Posted: 15 December 2022 doi:10.20944/preprints202212.0284.v1

Region	RA (h)	Dec (deg)	Area (sq deg)	Total Count	Density (gals/sq deg)
NGC	8 – 16	0 – 60	5,954	562,196	94.42
SGC	-2 – +2	0 – 30	859	59,925	69.76

Table 1. Parameters for the SDSS number count surveys (redshift$\leq$ 0.4, $b_J \leq 20$). J2000 equatorial coordinates

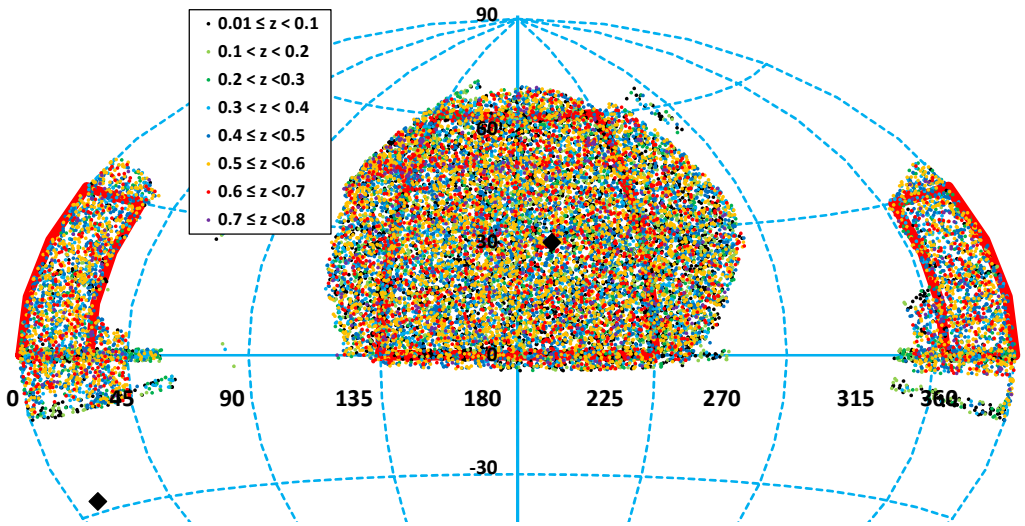

Figure 1. Aitoff-Hammer projection of areas covered from the SDSS (red boundaries). The galaxies observed are coloured according to their redshifts. The solid diamonds locate the North and South Galactic Centres (NGC and SGC).

SDSS surveys for this paper: a) The area centred on the North Galactic Centre (NGC), and b) an area above the South Galactic Centre (SGC) (Figure 1 and Table 1), using J2000 equatorial coordinates. The count limits were redshift $z \leq 0.4$, and $b_J \leq 20$. Cross-referencing historical magnitude systems with more recent filters such as those of the SDSS is not a trivial problem [3], as the earler B-filters were calibrated on stars based on the Johnson-Cousins UBVRI System, indicated generally by B_J. Conversion to this system from the SDSS was performed from the g' and r' bands empirically using $b_J = g + 0.155 + 0.152 * (g - r)$ [4], with appropriate de-reddening corrections and k-corrections [5].

The counts for the smaller SGC area are lower than those for the NGC area (Figure 2), but also suggest there is a lower density of galaxies in the SGC area compared with the NGC area with a deficit of 26% out to a redshift $z \sim 0.15$ (Figure 3), consistent with a local fluctuation of 2σ in large scale structure. A model for an extensive void was developed by Busswell *et al.* [6] who found evidence that the Southern counts with $B < 17$ mag were down by $\sim$ 30% out to $z = 0.1$ relative to the Northern counts from 2dFGRS, and this appeared to be relatively homogeneous over its whole range suggesting this could be modelled with a variable Φ^*, although this is not analysed further in this paper. Figure 2 shows the expected number count profile with limited b_J and redshift.

3. Calculating the observed volume

Number counts are determined in increments of apparent magnitude or half-magnitude per square degree of observed sky, but space is curved through the expansion of the universe, and the intrinsic luminosity and density of galaxies is not uniform [7]. Because magnitude is a function of luminosity distance (D_L), whereas the observable area is a function of diameter distance (D_A), the volume increment must be parameterised in z, producing a wineglass-shaped observable volume (Figure 4). The volume element/sterad is:

Preprints (www.preprints.org) | NOT PEER-REVIEWED | Posted: 15 December 2022 doi:10.20944/preprints202212.0284.v1

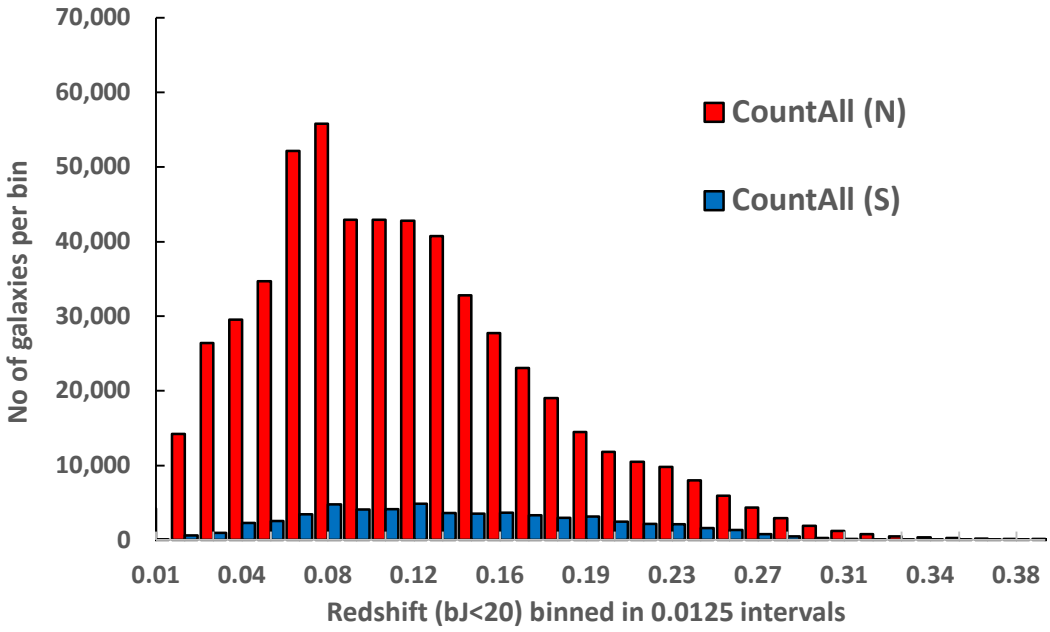

Figure 2. SDSS Number counts to (NGC and SGC, $z \leq 0.4$, $b_J \leq 20$). z-bins of 0.0125

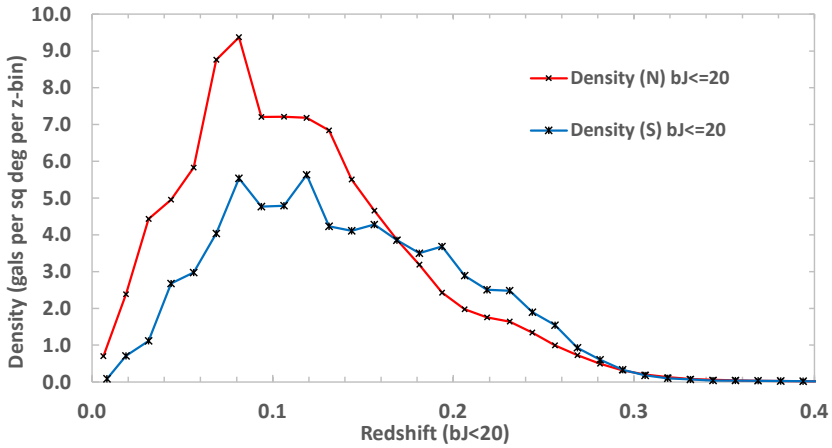

Figure 3. SDSS Galaxy density, NGC (red line) and SGC (blue line). $b_J \leq 20$, z-bins of 0.0125

Preprints (www.preprints.org) | NOT PEER-REVIEWED | Posted: 15 December 2022 doi:10.20944/preprints202212.0284.v1

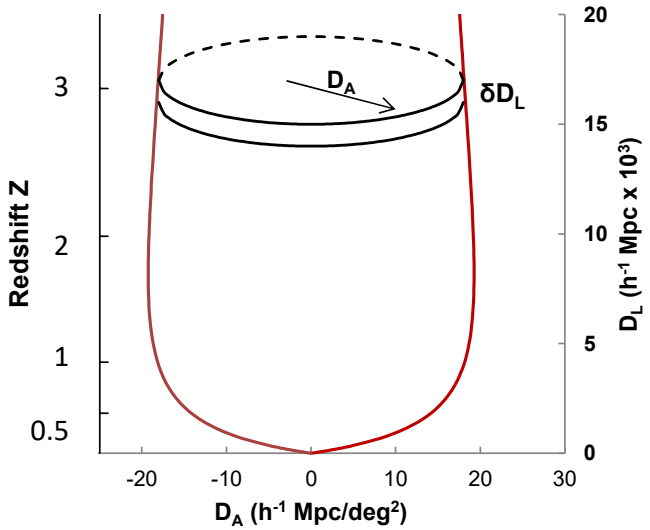

Figure 4. The observed volume/sq deg

$$\delta V = D_H^3 D_A^2 \delta D_L \,, \tag{1}$$

and

$$\begin{aligned} D_H &= c/H_0 \\ D_A &= D_C/(1+z) \\ D_L &= D_C(1+z) \end{aligned} \tag{2}$$

where D_H is the Hubble distance, D_A is the angular diameter distance and D_L the luminosity distance. D_C is the line-of-sight comoving distance, generally obtained by integrating the comoving equation for a Λ-Cold Dark Matter (ΛCDM) line-of-sight model derived from general relativity (GR), and involving terms for dark matter and dark energy. Here, the curvature term is derived from a model for GR incorporating the curvature of light across an expanding Universe [8]. With $\Omega_0 \simeq 0.28$ as the baryonic mass, this model was shown to closely approximate a standard ΛCDM model for angular diameter distances derived from baryonic oscillation (BO) data, and for luminosity distances derived from extensive super nova (SNe 1a) data, and by letting $\Omega_\Lambda = 0$ and assuming the intrinsic curvature term $\Omega_K = 0$, this has an analytical solution in z (Eq. 3):

$$D_C = \frac{1}{\sqrt{1-\Omega_m}} \log\left(\frac{(1+z)\left((1-0.5\Omega_m) + \sqrt{1-\Omega_m}\right)}{1+0.5\Omega_m(z-1) + \sqrt{(1-\Omega_m)(1+\Omega_m z)}} \right) \tag{3}$$

δV may now be expressed for the GR-model in terms of z as:

$$\delta V = D_H^3 \frac{D_C^2}{(1+z)^2} \frac{d}{dz}[D_C(1+z)]\delta z \; h^3 \; \mathrm{Mpc}^3 \;\; \mathrm{sterad}^{-1} \tag{4}$$

while the density function must be multiplied by a further factor of $(1+z)^3$ to allow for the contraction of space in three dimensions with look-back time. Integrating to a final redshift distance, z_{max}, then gives the total volume per sq. degree. The number of galaxies per Mpc per sq deg per magnitude increment is then:

$$n(m) = D_H^3 h^{-3} (1/3283.8) \int_0^{z_{max}} \Phi_z(m) \delta V \, \mathrm{d}z \, \mathrm{d}m \,. \tag{5}$$

Preprints (www.preprints.org) | NOT PEER-REVIEWED | Posted: 15 December 2022 doi:10.20944/preprints202212.0284.v1

Band	ϕ^* (10^{-2} h^3 Mpc^{-3})	$M^* - 5\log_{10}$h	α
0.1u	3.26±0.40	-17.89±0.04	-0.94±0.09
0.1g	2.42±0.10	-19.34±0.02	-0.92±0.04
0.1r	1.69±0.06	-20.37±0.02	-1.03±0.03
0.1i	1.62±0.06	-20.78±0.03	-1.02±0.04
0.1z	1.47±0.05	-21.12±0.02	-1.07±0.03

Table 2. SDSS Schechter Function fits for $\Omega_0 = 0.3$ and $\Omega_\Lambda = 0$ Cosmology at $z = 0.11$ [17]

where $\Phi_z(m)$ is the luminosity function (Section 4). z_{max} is taken to be the volume limit for the integral but, like much else in magnitude-number count analysis, this limit may be debated. Results from the Wilkinson Microwave Anisotropy Probe (WMAP) suggest reionization at $z = 11 - 30$ [9], but an emission signature of broad and asymmetric Lyman-α emission may specify the redshift of the final stages of reionization, suggesting a redshift range $z = 6 - 9$ [10]. However, counts of bright galaxies at redshifts $z \sim 6$ by Lyman-break selection find too few luminous galaxies for their hot stellar populations to power reionization [11]. This makes the most likely culprits lower-luminosity galaxies, which may equate with the small, low-metallicity objects found in significant numbers at $z = 2 - 3$ and sometimes termed subgalactic [12].

4. The Schechter Luminosity Function (LF)

For a specific sample of galaxies, S, it is usual to refer to the luminosity distribution defined by Schechter [13] as $ns(L)$ galaxies per unit luminosity for the sample. For a given sample size, the volume of the sample will vary with the luminosity and can be defined as $V_s(L)$.

Then the number of galaxies in S in the luminosity interval δL centred on L is $n_S(L)\delta L$, and the luminosity function (LF) $\Phi_S(L)$ of the sample S has the units of number of galaxies per unit luminosity per unit volume and is defined as $\Phi_S(L) \equiv \Phi(L)\delta L\ V_S(L)$ which is reached in the limit of $V_S(L) \to \infty$. Schechter defined his luminosity function as

$$\Phi(L)\,\mathrm{d}L = \Phi^*(L/L^*)^\alpha \exp\left(-L/L^*\right)\mathrm{d}(L/L^*) \tag{6}$$

but it is more useful to rewrite Eq. 6 in terms of absolute magnitude M^*:

$$n_S(M)\,\mathrm{d}M = \Phi^* V_C K \,\mathrm{dex}[0.4(\alpha+1)(M^*-M)]\exp[-\mathrm{dex}[0.4(M^*-M)]]\,\mathrm{d}M \tag{7}$$

Although there is considerable variation in the actual parameters, the Schechter function has received good experimental confirmation and there has also been some theoretical justification from a model of the non-linear matter distribution of rich clusters and their correlations, showing that the luminosity function has the Schechter form [14]. Nevertheless the actual form of the Schechter function is an amalgam of galaxies of many types, ages and distances and prone to wide variation, and it has therefore been continuously refined for several band-passes and galaxy types. Folkes et al. attempted to define the function in terms of spectral type from the 2dF Galaxy Redshift Survey, finding a range of values for the three parameters, M^*, ϕ, and α [15], and Metcalfe et al described Schechter parameters for five different galaxy types (E/S0, Sab, Sbc, Scd and Sdm), to produce a composite function [16].

The work of Schechter and others to determine a luminosity function for galaxies distributed randomly through space has been continuously refined for several band-passes and galaxy types, such as those of Blanton et al who used data from the extensive Sloane Digital Sky Survey (SDSS) data to define Schechter curves for five observational bands ($^{0.1}$u, $^{0.1}$g, $^{0.1}$r, $^{0.1}$i, and $^{0.1}$z) within a tight band of redshift at $z = 0.11$, for a number of cosmological models [17]. Their values for a Friedmann-Robertson-Walker (FRW) cosmo-

Preprints (www.preprints.org) | NOT PEER-REVIEWED | Posted: 15 December 2022 doi:10.20944/preprints202212.0284.v1

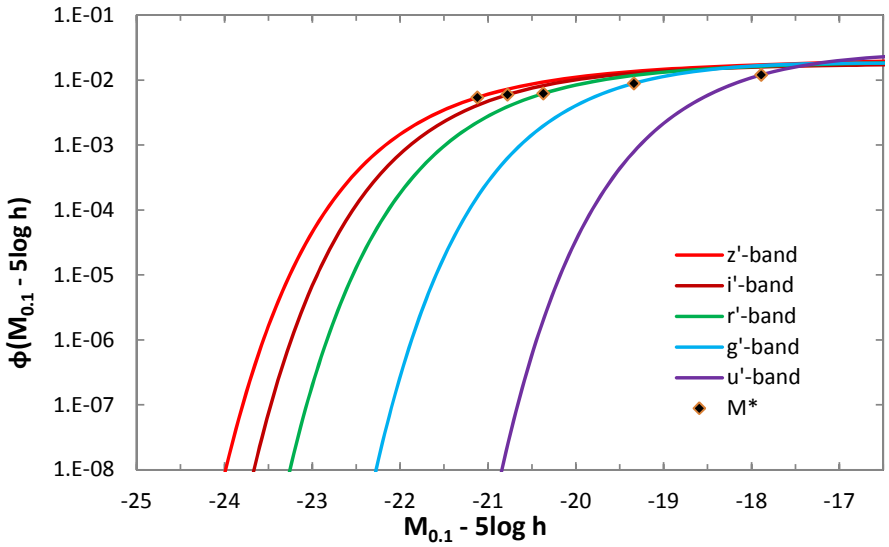

Figure 5. Schechter curves for 5 bands at uniform redshift ($z = 0.11$), after Blanton *et al.* [17].

logical world model with assumed matter density $\Omega_0 = 0.3$, vacuum pressure $\Omega_\Lambda = 0$, and Hubble constant $H_0 = 100$ h km s^{-1} Mpc^{-1} are presented graphically (Figure 5) and summarised in Table 2.

Blanton's results provide consistent and detailed parameters for the colour bands they selected and, although they do not provide a subdivision by galaxy type, they have the advantage of uniformity in their selection by sampling a well-defined shell at a fixed galactic distance. It may be noted that the curves in all bands are essentially flat at the faint end, corresponding to $\alpha \sim -1.0$.

5. Deriving the number count curves

The absolute magnitude M to produce each band of apparent magnitude m over the range of D_L is derived from the definition of D_L in the chosen GR model:

$$M = m - 5\log_{10}(D_L) - 25 \tag{8}$$

where $D_L = D_H(1+z)D_C$ for the appropriate GR-model. $n(m)$ is then derived by substituting for M in $\phi(z)$ in Eq. 5, and integrating Eq. 5 to z_{max} and over the range $m \pm 0.5$ per magnitude interval (or $m \pm 0.25$ per half-magnitude interval). It may be demonstrated by analysis that the resultant curve is an asymmetric hyperbola (Figure 6) with two distinct asymptotic slopes: the classical $\mathrm{d}\log_{10} N/\,\mathrm{d}m = 0.6$ Euclidean slope at bright magnitudes, and a slope of $-0.4(\alpha+1)$ at faint magnitudes. Normalisation over the Euclidean region is determined by ϕ^* and M^*. The asymmetric point of inflexion is a function of M^* and $\log(z_{max})$ that may be determined by numerical computation, but approximates to:

$$m_{inflexion} \simeq M^* + 2.5\log(z_{max}) + \text{constant}\,. \tag{9}$$

These contributions assume pure Schechter curves and make no allowance for evolution. In practice, they will show some change with redshift due to evolution from events such as starbursts, luminosity evolution and mergers, making the true underlying cause for any change in slope difficult to identify. Additionally, the observed counts may tail off at the faintest magnitudes, which would depress the faint end of the resultant curve. It may be noted that the curves in all bands of Figure 5 are essentially flat at the faint end, corresponding to $\alpha \simeq -1.0$. Such flat luminosity function (LF) curves give rise to very shallow number count curves which do not reflect reality. To account for the observations, there must be evolution of some or all components of the LF with increasing redshift, as

Preprints (www.preprints.org) | NOT PEER-REVIEWED | Posted: 15 December 2022 doi:10.20944/preprints202212.0284.v1

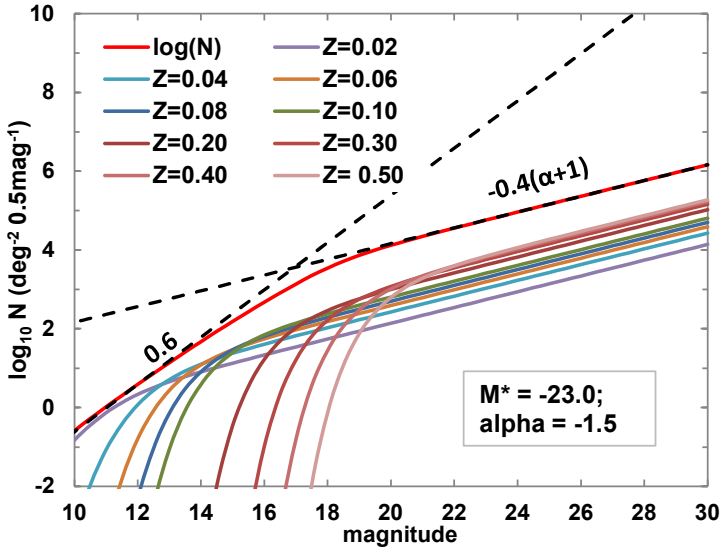

Figure 6. Building a theoretical number count curve (red line) with composite Schechter curves at increasing redshifts. The transition from a Euclidean slope of 0.6 to the α-dependent slope is clearly shown (dashed lines). ($M^* = -23.0; \alpha = -1.5$).

shown in Figure 6. This demonstrates how each observation redshift band combines to form the single composite curve, with $\alpha = -1.5$.

6. The observational data

Extensive number count data for six principle observational bands, ultraviolet ($U-$), blue ($B-$), red ($R-$), and infrarad ($I-$, $H-$, $K-$), with Effective Wavelength Midpoint (λ_{eff}) for each standard filter at 365nm, 445nm, 658nm, 806nm, 1630nm, and 2190nm respectively, are provided at the Durham Number Count Survey site [1]. Composite counts have been compiled by Jones *et al.* [18], Metcalfe *et al* [16,19–21] and McCracken *et al.* [22] from the many sources listed in the original tables, with the magnitude distribution modelled and averaged for each morphological type across the series.

The counts were integrated for apparent magnitude across a given viewing angle, defining a volume of redshift space per square degree. However, as described in Section 3, this volume is only Euclidean over small redshifts; as the counts probe deeper, the volume contained in each interval of redshift begins to shrink with increasing look-back time as observations come from earlier epochs of an expanding Universe, with additional corrections made for luminosity evolution and mergers and the increasing density of galaxies within a reducing volume. A typical composite curve for the number counts may then be constructed as in Figure 7 using K-data from the Durham compilation [23].

6.1. K-band magnitude count

The standard way to present the data for number counts is to show individual surveys overlapping along the curve. A more compact way to show these data is presented in Figure 7, where each series is binned into bins of $0.5mag$, with the mean of each bin plotted from a total of 41 published surveys. The data for the K-magnitude number counts demonstrate the theoretical asymmetric hyperbola of the model (Figure 6) almost exactly, with an inflexion at $mag_K \simeq 17.25$. The error bars are not RMS errors, but show the range of counts in each bin from the different surveys.

The picture of a steepening α with redshift may be fundamental to reconciling the steep observed slopes of the number counts at faint magnitudes to the flatter LF's reported at the present epoch (or $z = 0.11$ for the SDSS data), as shown by the solid red curve where

Preprints (www.preprints.org) | NOT PEER-REVIEWED | Posted: 15 December 2022 doi:10.20944/preprints202212.0284.v1

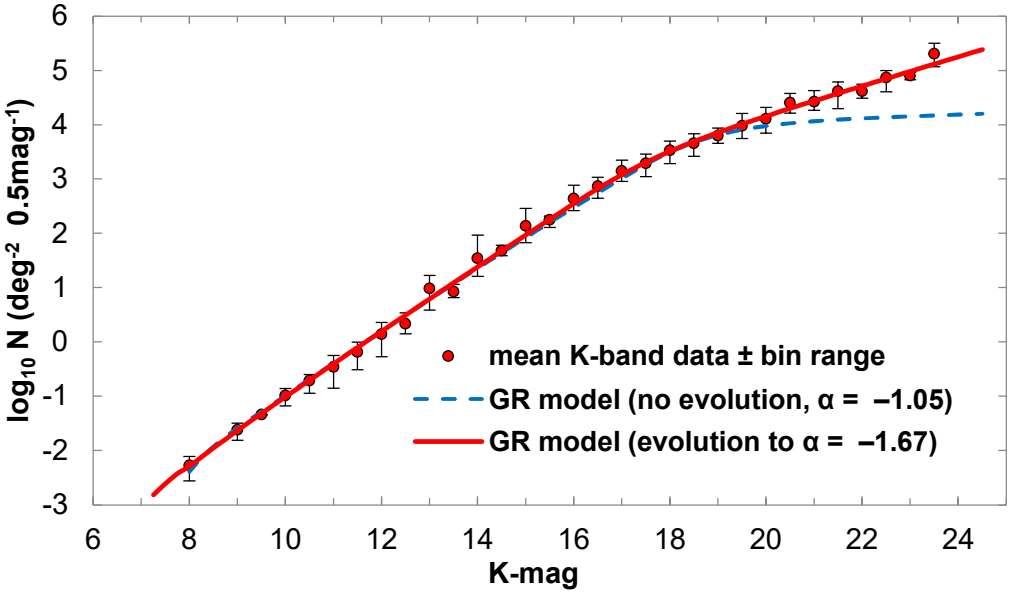

Figure 7. K-magnitude plots with no evolution (dashed line, $\alpha = -1.05$) and pure luminosity evolution (PLE) from $\alpha = -1.05$ to $\alpha = -1.67$ (solid line) in the GR model. The error bars reflect the range of each bin; the absence of error bars implies the bin has a single member. (Adapted from composite means of 39 K-band surveys from Durham number count archive, [23])

pure luminosity evolution (PLE) is represented by an increase in α from -1.05 to -1.67. For comparison, the green dashed curve shows the flatter $\alpha = -1.05$ with no evolution.

There is still some controversy about the best parameters to use when building these models. Gardner *et al.* [24] presented an early determination of the near-infrared K-band luminosity function for field galaxies from a wide-field K-selected redshift survey, suggesting that K-band surveys present a different picture from optical surveys: instead of rapid evolution at intermediate or even low redshifts, the counts and colours of the galaxies making up the K-band surveys show only passive evolution of the old stellar population to $z \sim 0.5$. Their best-fit Schechter function parameters with K-correction were: $M^* = -23.51$, $\alpha = -1.09$, and $\Phi^* h^{-3} = 1.5 \times 10^{-2}$ for the GR model. De Propris *et al.* [25] suggested brighter M^* but low alpha, such as $M^* = -24.63$ to -24.48 and $\alpha = -0.21$ to -0.81, while Huang *et al.* [26] determined $M^*(K) = -23.57 \pm 0.08 + 5 \log h$, $\alpha = -1.33 \pm 0.09$ and $\Phi^* = 0.017 \pm 0.002 h^3$ Mpc^{-3} for a universe with $\Omega_0 = 0.3$ and $\Omega_\Lambda = 0$, and Kochanek *et al.* [27] suggested $M^* = -23.39 - 5 \log h$; $\alpha = -1.09$; $\Phi^* = 1.16 \times 10^{-2}$ h^3 Mpc^{-3}.

A pure luminosity evolution (PLE) model was fitted to Figure 7 where the solid line shows the best fit for the GR-model using a single Schechter model with Kochanek's parameters and modest PLE up to $z = 0.5$, with α increasing with redshift from -1.05 to -1.67 and $M^* = -23.3$ for $H_0 = 70$. The curve was normalised in the Euclidean part of the plot at $mag_K = 12.0$ to the Frith 2MASS data points. It may be noted that the resulting plots are quite tight, and this binned representation is also used to show the remaining bands (Figures 8-12).

6.2. H-band

The H-band data (Figure 8), also plotted in bins of $0.5mag$, are from 14 surveys. The GR model with PLE shows a similar inflexion to the K-band, but with a flattening tail at faint magnitude ($H_{mag} \sim 25$), with $M^* = -23.5 - 5 \log h$; $\alpha = -1.07$, and PLE beyond $z = 0.52$. The curve was again normalised to the Frith 2MASS (2006) points, which show a good Euclidean fit. The tail comes from cutting the integration limit at $z = 2.5$, but the plots can also be fitted to this tail using the values of Kochenek [27] with $M^* = -23.9$; $\alpha = -1.03$

Preprints (www.preprints.org) | NOT PEER-REVIEWED | Posted: 15 December 2022 doi:10.20944/preprints202212.0284.v1

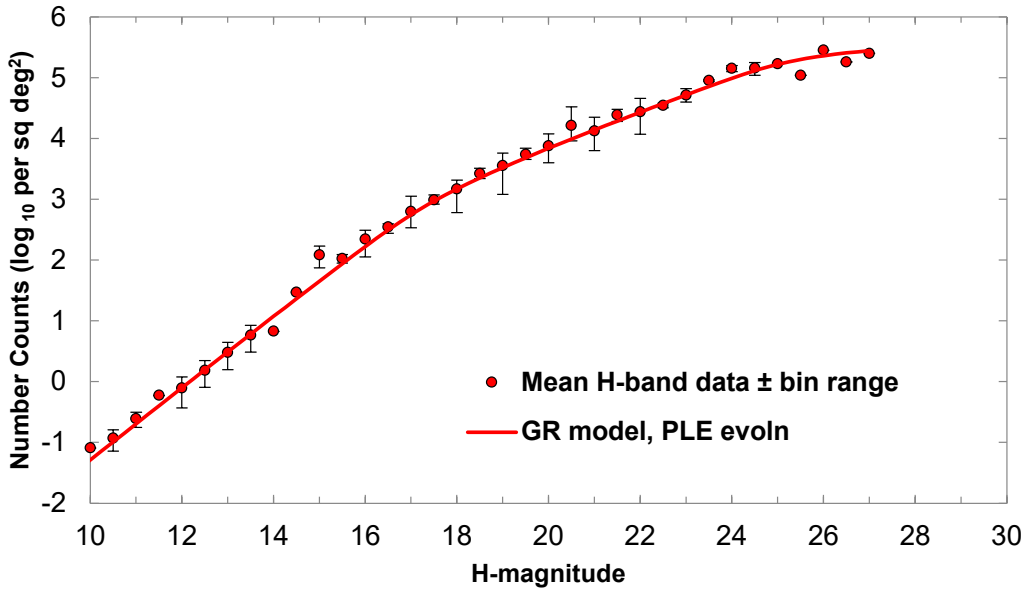

Figure 8. H-magnitude plots, GR model with PLE (solid line).Adapted from composite means of 14 H-band surveys (Durham number count archive [1])

and integrating out to $z = 2$. Further data beyond $H_{mag} = 27$ may determine if the tail is real, or if the true counts continue to rise.

6.3. I-band

The I-band data (Figure 9) is from 26 surveys and show a gentle inflexion with a tailing off beyond $I_{mag} \sim 26$. The GR model mimics the data well with $M^* = -21.00 - 5\log h$; $\alpha = -1.0$; $\Phi^* = 0.0328h^3$ Mpc^{-3} as quoted in the SDSS paper (Blanton 2002), and a PLE term of $(z+1)^{\beta}$ with $\beta = -0.15$. As with the H-band plots, a good fit is obtained to the tail by limiting the integration to $z = 2.0$.

6.4. R-band

The R-band data, taken from 31 surveys, show an inflexion at $R_{mag} \sim 24$, with a slight tail-off at faint magnitude ($R_{mag} \sim 27$). Using the SDSS survey values $M^* = -20.37 - 5\log h$; $\alpha = -1.03$; $\Phi^* = 0.0169h^3$ Mpc^{-3} with a PLE model at $z = 0.85$, $\beta = -0.16$ and $H_0 = 70$, the model mimics the data reasonably well with modest PLE (Figure 10).

6.5. U-band

The U-band data, taken from 19 surveys, has a wide spread over much of its range, with an inflexion beyond $U_{mag} > 25$. The curve suggests there may be mild starburst activity at $\sim 21mag$, but a simple PLE model with $M^* = -22.3 - 5\log h$ and $\alpha = -1.20$, integrated out to $z - 3.0$ with $\beta = 0.07$, $\gamma = 1.0$, also lies within the spread of the series (Figure 11).

6.6. B-band

Figure 12 summarises the b_J number counts by binning them in half-magnitude bins with the error bars showing the range of data in each bin, The absence of an error bar implies that the bin contains only a single data point. Ellis [28] described the B-band curves as an apparent excess of faint blue galaxy counts over the number expected on the basis of local galaxy properties; this has been referred to collectively as the faint blue galaxy problem [29], and is evident in Figure 12, taken from 36 $B-$band surveys. Metcalfe *et al.* [20] presented number count data with a blue magnitude limit of $B_{ccd} = 27.5$ mag showing that, for high q_0, it was not possible to reconcile the slope and numbers of galaxies

Preprints (www.preprints.org) | NOT PEER-REVIEWED | Posted: 15 December 2022 doi:10.20944/preprints202212.0284.v1

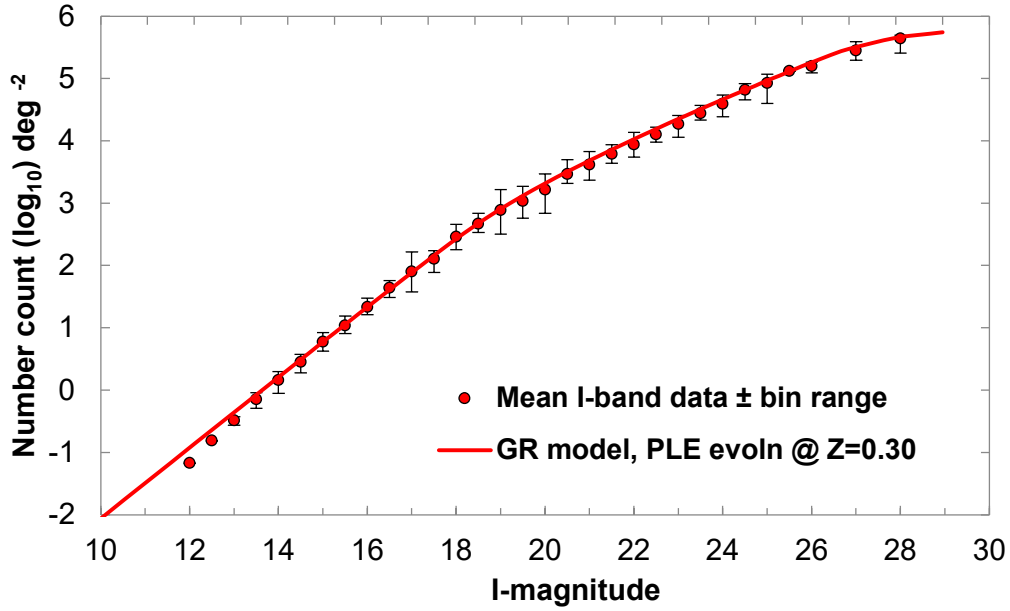

Figure 9. I-magnitude plots with PLE (solid line) in the GR model.(Adapted from composite means of 26 I-band surveys from Durham number count archive, [1])

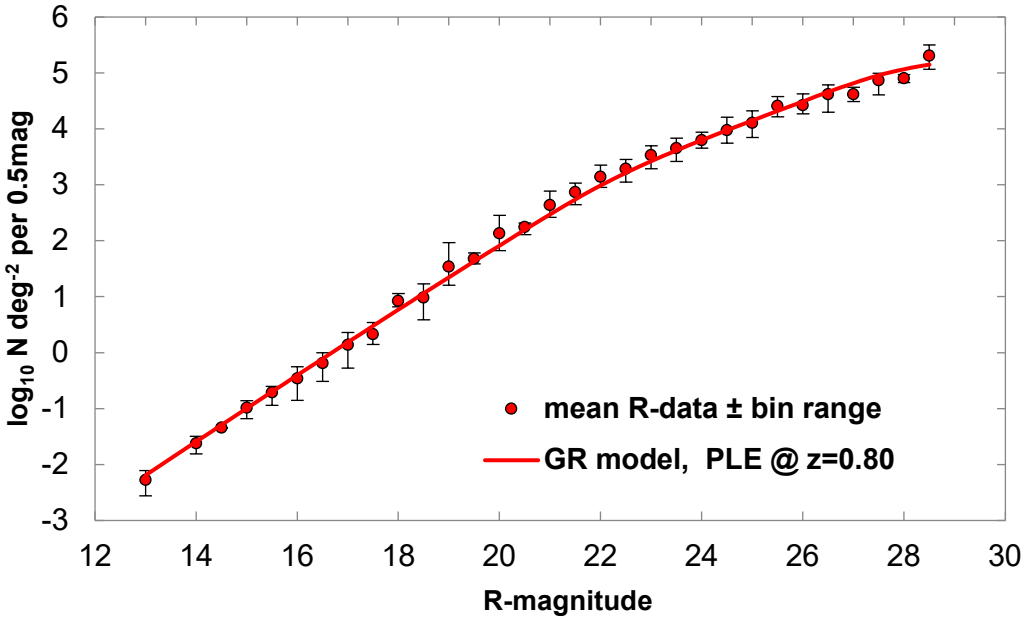

Figure 10. R-magnitude plots with PLE (solid line) in the GR model.(Adapted from composite means of 31 R-band surveys from Durham number count archive, [1])

Preprints (www.preprints.org) | NOT PEER-REVIEWED | Posted: 15 December 2022 doi:10.20944/preprints202212.0284.v1

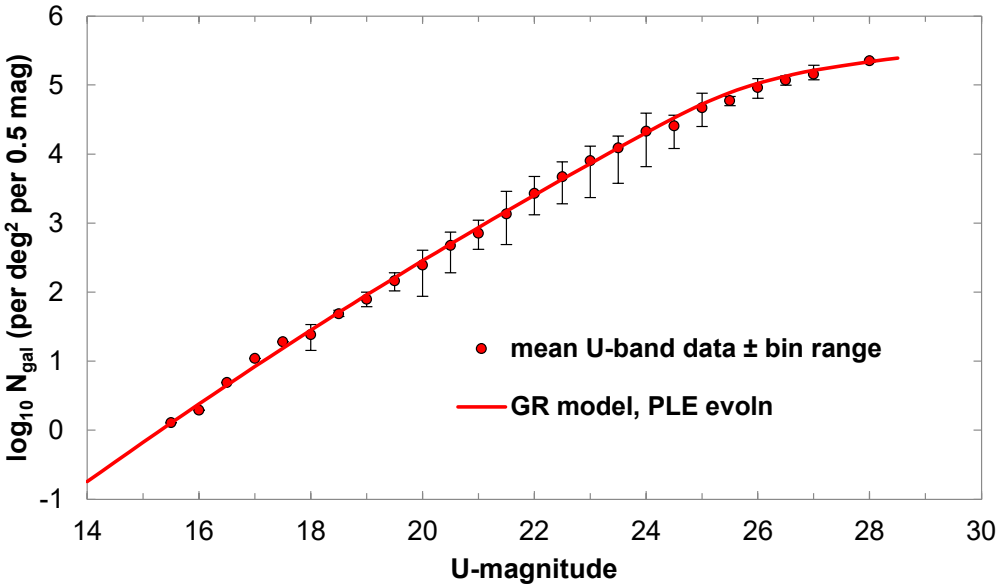

Figure 11. U-magnitude plots with PLE (solid line) in the GR model.(Adapted from composite means of 19 U-band surveys from Durham number count archive, [1])

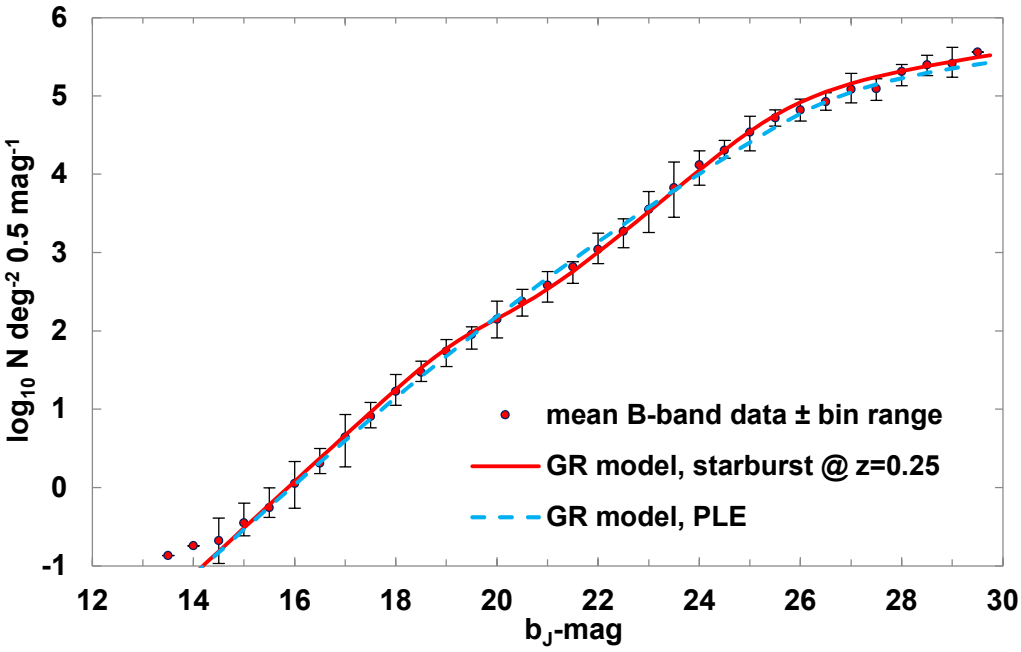

Figure 12. B-band magnitude counts binned (composite mean of 36 B-band surveys). (a) GR model with starburst evolution beyond z>0.25 (Solid line); (b) PLE (Dashed line). Both with $\alpha = -1.21$, $M^* = -19.66$. Adapted from Durham number count archive [1].

Preprints (www.preprints.org) | NOT PEER-REVIEWED | Posted: 15 December 2022 doi:10.20944/preprints202212.0284.v1

Param	K	H	I	R	B	U
α	-1.07	-1.07	-1.02	-1.03	-0.92	-0.94
M^*	-21.12	-21.12	-20.78	-20.37	-19.34	-17.89
z_{max}	1.00	1.20	2.00	2.00	2.30	1.10
ϕ^*	0.2920	0.1430	0.0286	0.0219	0.0124	0.1292
m_{norm}	12.00	12.00	14.00	14.00	18.00	18.00
β	-0.350	-0.330	-0.160	-0.140	-0.090	-0.200
$z_{evo'n}$	0.180	0.180	0.180	0.150	0.100	0.100

Table 3. Schechter and PLE parameters for the six pass bands of Figure 13, adapted from the SDSS parameters of Blanton *et al.* [17] ($H_0 = 100\ h\ km\ s^{-1}\ Mpc^{-1}$ with $h = 1$).

at $B > 25$ with the slope of the local faint galaxy luminosity function unless this was steeper in the past, or density evolution had taken place [19]. Norberg *et al.* [4] performed a detailed analysis of more than 110,500 galaxies from the 2dF Galaxy Redshift Survey (2dFGRS) to generate a luminosity function (LF) standardised to $z = 0$. Over the interval $-16.5 > M_{b_J} - 5\log h > -22$, their LF is accurately described by a Schechter function with $M_{b_J} - 5\log h = -19.66 \pm 0.07$, $\alpha = -1.21 \pm 0.03$ and $\Phi^* = 1.61 \pm 0.08 \times 10^{-2}\ h^3$ Mpc^{-3}; in broad agreement with earlier calculations by Yasuda et al [30].

Modelling the number count curves in the $B-$band is confounded in part because of the ability to fit several different models to the same data by varying the parameters, and alternative models with starburst evolution, an extensive void, PLE, and a two-galaxy type composite model can all be adjusted to a reasonable fit [7]. Curves for the GR starburst model (solid line) and a PLE model (dashed line) are shown in Figure 12, with $M^* = -19.66 - 5\log h$; $\alpha = -1.25$; $\Phi^* = 0.0125h^3$ Mpc^{-3}. The steeper rise seen in the observed data implies a more intensive rate of evolution as suggested in the starburst model (red solid line), which uses Norberg's values with a starburst of $M^* = +1.0$ occurring beyond redshift $z > 0.25$. The rate of PLE has been adjusted to compensate for the under-density from $20 < B_{mag} < 22.5$, otherwise the over-density would be considerably more severe and, although the PLE model appeared to give the best fit at the faint end, this model lacks the abrupt rise and gave the poorest overall fit to the B-data, resulting in an over-prediction in the range $-20 < B_j < 24$.

6.7. Number counts observational data summary

If all six bands of Figures 7-12 had viewed the same galaxies, then the number counts ought to be identical over the brightest regions where the curves are still purely Euclidean and visible across all bands. Taking the K-band curve as the reference curve, the remaining bands were therefore normalised to this by taking the inflexion point of the Euclidean slopes as a common point (Figure 13) to perform an inter-band comparison of the mean counts and their model curves. The assumed initial values for M^* and α for the model curves were fitted to the GR model using the SDSS data of Blanton *et al.* [17], assumed to be correct at $z = 0.1$ (Table 3), with Φ^* adjusted to normalise the curves to the observational $K-$band data. All curves were fitted by varying the rate of luminosity evolution, β. For consistency, the $B-$ and $U-$band theoretical curves have PLE correction only, without attempting to obtain the better fits seen with the starburst models.

The different rates of evolution in past epochs, which appear to have gradually increased with decreasing observational wavelength from the $K-$ to $U-$bands, and the excess in numbers of the $U-$ and $B-$bands is clearly evident. Also evident is a regular increase in counts from the $K-$band through the $R-$band up to the $B-$ and $U-$bands, with an excess in the $U-$band $> 24mag$. These curves are each integrated out to high redshift, but the slight downward tail at the faint end of some of the curves originates from limiting the redshift to which the curves are integrated to match the data. The essential features of these curves are:

Preprints (www.preprints.org) | NOT PEER-REVIEWED | Posted: 15 December 2022 doi:10.20944/preprints202212.0284.v1

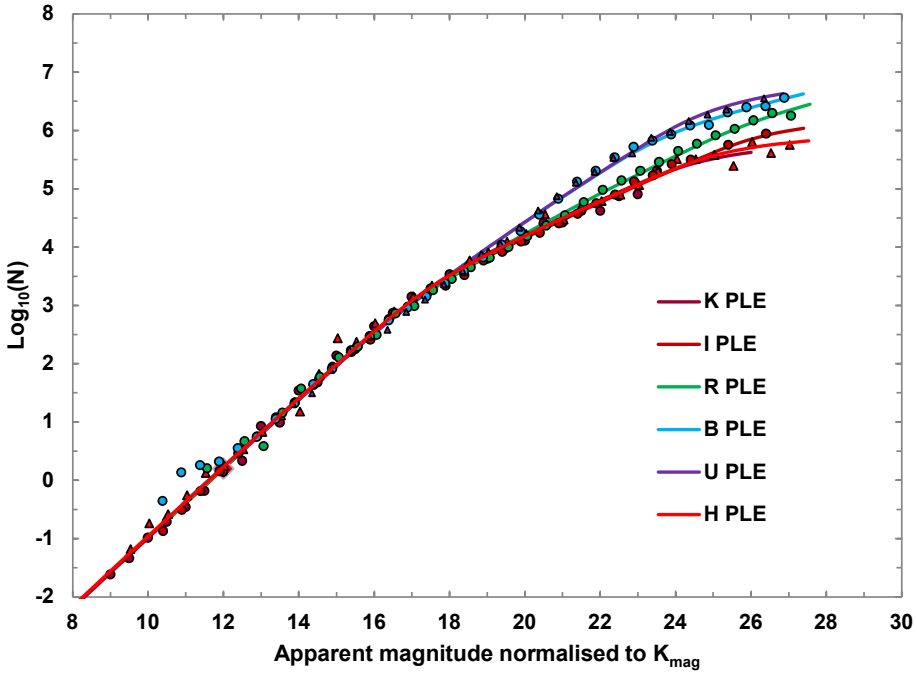

Figure 13. Mean data from the 6 photometric bands of Figures 7-12 with overlain curves assuming PLE. Normalised to $K-$mag curve to show change in faint slope with colour band. Bin ranges have been omitted for clarity. (Data adapted from [1]).

1. All the bright-end slopes match the predicted Euclidian slope of 0.6
2. The measured galaxy number counts (GNCs) generally increase with decreasing photometric wavelength
3. The $K-$ $H-$ $I-$ and $R-$bands require no additional evolutionary factors, although evolutionary variation in Φ^* and α may be accommodated within the models
4. The $B-$ and $U-$band curves require additional evolution to account for the excess counts at faint magnitude. To a first approximation, a simple starburst model with an increase in absolute M^* is sufficient to account for this

7. Evolutionary effects on the LF

The need for faster rates of evolution in the b_J-band than the redder $R-$ or $K-$bands may be explained by a model for evolution whereby some types of galaxies radiated larger amounts of flux in the rest U-band relative to the redder passbands [31]. Metcalfe *et al.* [16] suggested a second peak at high redshift, possibly explained by a sub-population of early-type galaxies with ongoing star formation. This model has received support from McDonald *et al.* [32] who reported X-ray, optical and infrared observations of the galaxy cluster SPT-CLJ2344-4243 at redshift $z = 0.596$ that reveal an exceptionally luminous galaxy cluster that appears to be experiencing a massive starburst, with a formation rate of ~ 740 solar masses per year. Atek *et al* have probed the UV LF to $z \sim 7$, computing each field individually and comparing their results to the compilation of the *HST* legacy fields, the LF fields and the UDF12 field [33]. The underlying physical cause for these rapidly evolving galaxies appears to be related to their star-formation rates. Galaxies with the strongest [O II] emissions dominate the evolutionary trends and their luminosity density has fallen by a large factor since $z \sim 0.5$ [34]. At the present epoch, such systems all lie at the faint end of the LF, but even at modest redshift they occupy a wide range of luminosities. Cohen [35] reported that E galaxies become more luminous by $z \simeq 1$ with the mean star formation rate (SFR) increasing strongly between $0 \leq z \leq 1$, by a factor of ~ 10. The most luminous galaxies showed this trend very strongly, but Cohen reported only modest evolution of M^*

Preprints (www.preprints.org) | NOT PEER-REVIEWED | Posted: 15 December 2022 doi:10.20944/preprints202212.0284.v1

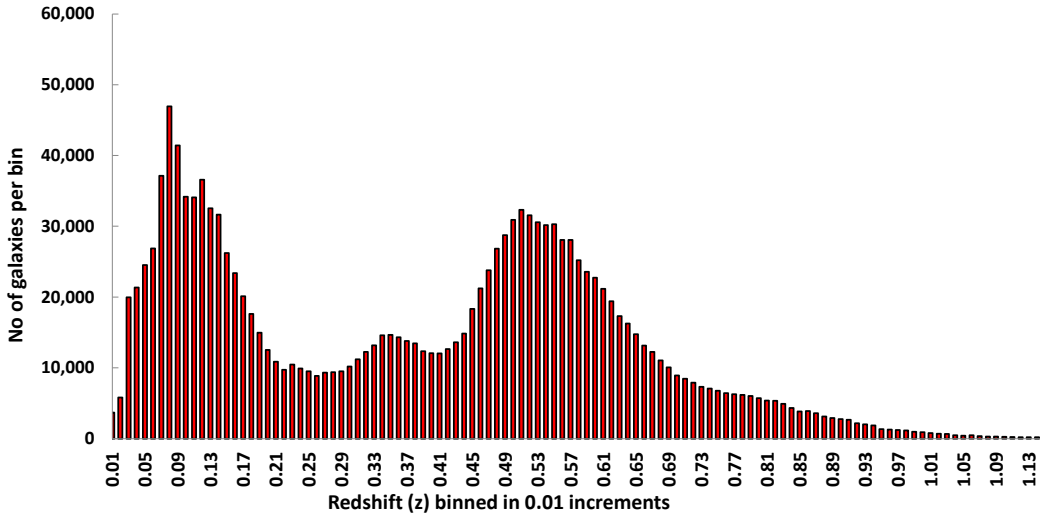

Figure 14. Extended SDSS Number counts (NGC, $z \leq 1.20$, $b_J \leq 24$)

with z, consistent with passive evolution but with no evidence for a large increase with z in the rate of major mergers. At the faintest magnitudes, the observed counts tail off, which depresses the faint end of the resultant curve.

Arnouts *et al.* [36] presented measurements of the galaxy LF at 1500Å in the range $0.2 \leq z \leq 1.2$ based on Galaxy Evolution Explorer VIMOS-VLT Deep Survey observations for 1000 spectroscopic redshifts, and at higher z using existing data sets. Their main results were: (a) Luminosity evolution is observed with $\Delta M^* \sim -2.0$ mag between $0 \leq z \leq 1$ and $\Delta M^* \sim -1.0$ mag between $1 \leq z \leq 3$, confirming that star formation activity was significantly higher in the past. (b) The LF slopes vary in the range $-1.2 \geq \alpha \geq -1.65$, with possibly further increase at higher z. (c) Analysis of three spectral type classifications, Sb-Sd, SdIrr, and unobscured starbursts, found that, although the bluest class evolved less strongly in luminosity than the other two classes, their number density increased sharply with z from $\simeq 15\%$ in the local universe to $\simeq 55\%$ at $z \simeq 1$, while that of the reddest classes decreased.

7.1. Evolutionary effects on the LF from the SDSS

Possible causes for the 'faint blue galaxy problem' were considered using the Sloan Digital Sky Survey (SDSS) to explore the galaxy population at these fainter magnitudes. Historical number count data did not subdivide each magnitude bin into redshift bins, but the SDSS has provided a wealth of data, and currently lists details of more than one million galaxies across five spectral bands ($u-$, $g-$, $r-$, $i-$, $z-$) and includes spectral redshift data. For comparison with optical observations, the SDSS apparent magnitudes were converted to the optical B_J band, with corrections for extinction and k-corrections. Number count plots of the five SDSS bands confirmed a Euclidean slope of $N \propto 10^{0.6m}$ at bright magnitudes with a limiting inflexion point at an apparent magnitude that increased with wavelength.

Extending the SDSS number count range of Figure 2 to $z \leq 1.2$ and $b_J \leq 24$ suggested a significant secondary peak in redshift between $0.48 \leq z \leq 0.57$ with a maximum at redshift~ 0.51 (Figure 14). The effect of this on the total number-count curve is evident in Figure 15 which is the composite b_J curve derived from subdividing the magnitude bins into the individual redshift bands up to a maximum redshift $z \leq 1.20$. The secondary peak in counts is evident at redshifts beyond $z \geq 0.3$, although it must be emphasised that measurements are highly variable due to considerable inhomogeneity in the sky surveys and the incompleteness of the SDSS beyond the magnitude cutoff of each band, with progressively incomplete counts beyond these limits. This SDSS survey was conducted across a large area of sky, and subdivided the counts according to redshift. This contrasts

Preprints (www.preprints.org) | NOT PEER-REVIEWED | Posted: 15 December 2022 doi:10.20944/preprints202212.0284.v1

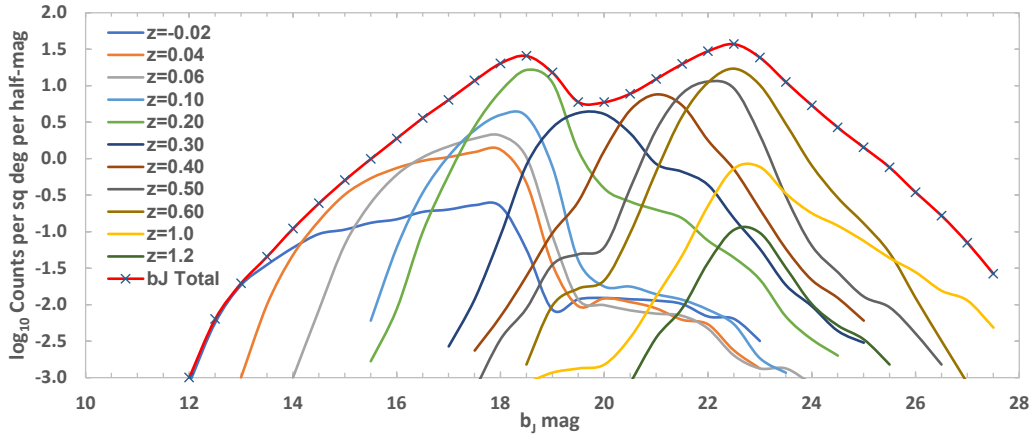

Figure 15. Contribution to b_J magnitude curve from each redshift cohort. ($z \leq 1.20$, $b_J \leq 28$)

with most earlier surveys which looked at a small, limited, area of sky and counted all galaxies irrespective of redshift.

A random sample of 100 galaxies between $0.49 \leq z \leq 0.51$ was cross-referenced with the astronomical database, *Simbad*. From a total of 64,915 galaxies at the secondary redshift peak, a majority were QSOs, irregular galaxies or giant elliptical galaxies. A few appeared to be misclassified as stars in *Simbad*, but as galaxies in the SDSS; some others had 'no object' recorded in Simbad. This may be a consequence of incompleteness in the catalogue, but a further problem may be inconsistent coordinates and classification of galaxy types across catalogues [37].

The types of sources making up the faint, sub-microjansky radio sky include star-forming galaxies (SFGs), radio-quiet active galactic nuclei, low radio power ellipticals and dwarf galaxies. Blanton *et al.* [38] found that most galaxies in the SDSS with low-redshift ($z < 0.05$) at the faint end of the LF are blue, and therefore most dwarfs in the Universe should be of the star-forming type with the same luminosity evolution as the SFGs [39]. Kellermann *et al.* [40] selected low-redshift SDSS quasi-stellar objects (QSOs) for an ultra-deep QSO survey. They suggested that the QSOs primarily comprise two components: (1) a small fraction of quasi-stellar object (QSO) galaxies with radio-loud active galactic nuclei (AGN) accreting into a central, supermassive black hole, characterized by their luminous, powerful radio emission; and (2) a large number of starburst-driven QSO host galaxies with a radio-quiet AGN population but an appreciable fraction of strong X-ray-emitting AGNs [41].

The Hubble Space Telescope (HST) Medium Deep Survey (MDS) found that the universe is dwarf-rich at $z = 0.3 - 0.5$ consistent with a dwarf luminosity function with a steep faint-end slope. The giant ellipticals and spirals have been relatively stable since $z \sim 0.7$, whereas there has been rapid evolution of the irregular galaxy population with an increasing number of irregular and peculiar systems with increasing magnitude, with clear evolution of the blue population and little or no evolution of the red population [42].

Starburst galaxies have an exceptionally high rate of star formation, up to 100 $M_\odot$ per year compared with an average rate of star formation of only $\sim 3M_\odot$ per year for a stable galaxy [43]. This was possibly driven by an epoch-dependent galaxy merger rate that caused a combination of starbursts and weak AGN activity up to $z \gtrsim 0.5 - 1.0$ [44]. Each of these populations evolved strongly in the past, and some support for this comes from the microJansky radio source population, thought to originate from a mixture of starburst, post-starburst and elliptical galaxies [44]. Owen *et al.* [45] has suggested there is also extensive starburst activity at very high redshifts ($z \geq 7$), with extreme X-ray luminosity to explain the rise in observable counts detected in the $B-$ and $U-$bands where the excess UV and X-ray emission is red-shifted into the blue and violet.

 doi:10.20944/preprints202212.0284.v1

8. Discussion

Galaxy number counts (GNCs) as a function of magnitude provided an early, straightforward quantity in cosmology, and numerous surveys have continued to increase the faint magnitude limit in six principle observational photometric bands. Although originally considered as a possible cosmological test, they are now seen to be more sensitive to galactic evolution than to the cosmological model, and Weinberg suggested that: "... in the interpretation of number counts, I find it hard to believe that it is possible to disentangle the effects of evolution" (Weinberg S. Personal communication), while Ellis [46] stated that, "although the original motivation was an attempt to quantify the cosmological world model, [this is now] concerned with the study of faint galaxies as a way of probing their evolutionary history". The problems are well understood, but present many difficulties in observational astronomy and continue to generate discussion about the corrections required. The problems in interpreting galaxy number counts may be summarised as:

1. At the bright end of the curves, local clustering and over-density distort the true Euclidian slope. This is particularly pronounced with the B_j counts brighter than mag $B_j < 14$.
2. The galaxy density distribution with absolute magnitude is unknown, but appears to depend on age and galaxy type. Number counts based on apparent magnitude bands include all galaxy types and ages, and galaxy types may also evolve at different rates [47].
3. The large redshifts of the more distant objects shift the observable spectra into less well characterised emission bands, which are approximated by tables of K-corrections, but these are confounded by the large uncertainties in how these spectra have evolved from the early universe.
4. There are large uncertainties in the reddening, dust extinction, evolution of bright cluster galaxies (BCGs), and mergers of smaller dwarf galaxies at high redshift [48].
5. The curves have a low dependence on α, but are very dependent on M^*, which clearly affects the results as counts are extended to redshifts at which galactic evolution becomes significant.
6. The actual number of galaxies/unit volume appears to continuously increase with decreasing absolute magnitude, within the observational limit. At the high surface density of objects found on these frames, corrections are made for field overcrowding (images overlapping) and for the efficiency of the detection and measurement software. In some surveys beyond $B \gtrsim 26$, some corrections applied were up to 10 times larger than the raw data [49].
7. Conversely, gravitational lensing may produce multiple images, again confusing the true number counts [50].

The observational data for galaxy number counts have been accumulated over many years from a variety of sources and across different sky fields, leading much of the data to have a wide spread. For this paper, the means of the data at each magnitude from all available surveys were plotted for each band. These were overlain with the theoretical curves using accepted values for absolute magnitude (M^*) and faint slope (α) in the Schechter function. The cosmological model selected is of less importance, as standard ΛCDM models can be fitted by changing the rate of evolution to match the model chosen [46]. A general relativity (GR) model was selected that has been shown to closely approximate both the luminosity distances derived from extensive SNe 1a data and angular diameter distances derived from baryonic oscillation (BO) data [8].

All curves were well characterised by a Euclidean slope $N \propto 10^{0.6m}$ at bright magnitudes, with an inflexion point whose apparent magnitude increased with wavelength, and whose faint end slope also increased with wavelength (Figure 13). The four reddest wavelengths ($K-$, $I-$, $R-$ and $H-$) each required a small pure luminosity evolution (PLE) term to produce a steeper faint slope to fit the observations. Only M^* was assumed to have evolved in these models, but in practice α and Φ^* also have evolved [21] and evolution rates probably vary over the lifetime of these galaxies. Number counts may also have

been higher in the past because there were more galaxies in past epochs, reducing through mergers to the present epoch. Although each galaxy type may have evolved with its own parameters and time scale, the Schechter models assumed for this paper followed the method of Blanton *et al.* [17] for the SDSS using composite values for each colour band. The curves describe the observations sufficiently well that additional discrimination of the parameters for M^* and α is not required. The two bluest wavelengths ($B-$ and $U-$) each showed a steep rise in their curves, particularly pronounced in the $B-$band. This required a starburst parameter for the $B-$band, but the rise in the $U-$band was sufficiently small that simple PLE could model it. The steeper curve of the $B-$band at faint magnitudes can be fitted well with only a small (≤ 1 mag) additional starburst correction to give a good fit over the whole range of observations.

Extending the northern SDSS counts to higher redshift and apparent magnitude limits showed a secondary peak in the counts at redshift~ 0.5, and more detailed examination of individual galaxies at this peak redshift confirmed that many were QSOs, AGN, irregular dwarfs, starburst galaxies, or giant elliptical galaxies. These are all active galaxies with high star-forming activity and correspondingly higher UV-emission leading to brighter absolute magnitudes (M^*) in the past [43,44].

Acknowledgments: I am indebted to Tom Shanks, Nigel Metcalfe, and Richard Ellis for their early support, to the Extragalactic Research Group of Durham University for collating and publishing the many observations, and to the SDSS team for making their data fully accessible.

Funding: This research received no external funding

Conflicts of Interest: The author declares no conflict of interest.

1. Durham Galaxy Number-Counts, 2010, [astro.dur.ac.uk/ nm/pubhtml/counts/counts.html]. Accessed: 2022-08-04.
2. Abdurro'uf.; Accetta, K.; Aerts, C.; Silva Aguirre, V.; Ahumada, R.; et. al.. The Seventeenth Data Release of the Sloan Digital Sky Surveys: Complete Release of MaNGA, MaStar, and APOGEE-2 Data. *ApJS* **2022**, *259*, 35, [arXiv:astro-ph.GA/2112.02026]. https://doi.org/10.3847/1538-4365/ac4414.
3. Bessell, M.S. Standard Photometric Systems. *ARA&A* **2005**, *43*, 293–336. https://doi.org/10.1146/annurev.astro.41.082801.100251.
4. Norberg, P.; Cole, S.; Baugh, C.M.; et al. The 2dF Galaxy Redshift Survey: the bJ-band galaxy luminosity function and survey selection function. *Monthly Notices of the Royal Astronomical Society* **2002**, *336*, 907–931, [https://academic.oup.com/mnras/article-pdf/336/3/907/2959521/336-3-907.pdf]. https://doi.org/10.1046/j.1365-8711.2002.05831.x.
5. Blanton, M.R.; Brinkmann, J.; Csabai, I.; Doi, M.; Eisenstein, D.; Fukugita, M.; Gunn, J.E.; Hogg, D.W.; Schlegel, D.J. Estimating Fixed-Frame Galaxy Magnitudes in the Sloan Digital Sky Survey. *AJ* **2003**, *125*, 2348–2360, [arXiv:astro-ph/astro-ph/0205243]. https://doi.org/10.1086/342935.
6. Busswell, G.S.; Shanks, T.; Frith, W.J.; Outram, P.J.; Metcalfe, N.; Fong, R. The local hole in the galaxy distribution: new optical evidence. *MNRAS* **2004**, *354*, 991–1004, [arXiv:astro-ph/astro-ph/0302330]. https://doi.org/10.1111/j.1365-2966.2004.08217.x.
7. Marr, J.H. Bright galaxy number counts. Master's thesis, Durham University, Durham, UK, 1995, [http://etheses.dur.ac.uk/5373/].
8. Marr, J.H. Hubble Expansion as an Einstein Curvature. *Journal of Modern Physics* **2022**, *13*, 969–991, [arXiv:physics.gen-ph/1803.02198].
9. Bennett, C.L.; Halpern, M.; Hinshaw, G.; et. al. First-Year Wilkinson Microwave Anisotropy Probe (WMAP) Observations: Preliminary Maps and Basic Results. *ApJS* **2003**, *148*, 1–27. https://doi.org/10.1086/377253.
10. Windhorst, R.A.; Taylor, V.A.; Jansen, R.A.; et. al. A Hubble Space Telescope Survey of the Mid-Ultraviolet Morphology of Nearby Galaxies. *ApJS* **2002**, *143*, 113–158. https://doi.org/10.1086/341556.
11. Lehnert, M.D.; Bremer, M. Luminous Lyman Break Galaxies at z>5 and the Source of Reionization. *ApJ* **2003**, *593*, 630–639. https://doi.org/10.1086/376729.

12. Yan, H.; Windhorst, R.A.; Cohen, S.H. Searching for z≃6 Objects with the Hubble Space Telescope Advanced Camera for Surveys: Preliminary Analysis of a Deep Parallel Field. *ApJL* **2003**, *585*, L93–L96. https://doi.org/10.1086/374371.
13. Schechter, P. An analytic expression for the luminosity function for galaxies. *ApJ* **1976**, *203*, 297–306. https://doi.org/10.1086/154079.
14. Schaeffer, R. Galaxies, Clusters and Fluctuations. In Proceedings of the Large Scale Structures of the Universe; Audouze, J.; Pelletan, M.C.; Szalay, A.; Zel'dovich, Y.B.; Peebles, P.J.E., Eds., 1988, Vol. 130, p. 215.
15. Folkes, S.; Ronen, S.; Price, I.; et. al. The 2dF Galaxy Redshift Survey: spectral types and luminosity functions. *MNRAS* **1999**, *308*, 459–472. https://doi.org/10.1046/j.1365-8711.1999.02721.x.
16. Metcalfe, N.; Shanks, T.; Weilbacher, P.M.; McCracken, H.J.; Fong, R.; Thompson, D. Galaxy number counts - VI. An H-band survey of the Herschel Deep Field. *Monthly Notices of the Royal Astronomical Society* **2006**, *370*, 1257–1273. https://doi.org/10.1111/j.1365-2966.2006.10534.x.
17. Blanton, M.R.; Hogg, D.W.; Bahcall, N.A.; et. al. The Galaxy Luminosity Function and Luminosity Density at Redshift z = 0.1. *ApJ* **2003**, *592*, 819–838. https://doi.org/10.1086/375776.
18. Jones, L.R.; Fong, R.; Shanks, T.; Ellis, R.S.; Peterson, B.A. Galaxy number counts. - I. Photographic observations to B=23.5 mag. *MNRAS* **1991**, *249*, 481–497. https://doi.org/10.1093/mnras/249.3.481.
19. Metcalfe, N.; Shanks, T.; Fong, R.; Jones, L.R. Galaxy number counts - II. CCD observations to B = 25 mag. *Monthly Notices of the Royal Astronomical Society* **1991**, *249*, 498–522. https://doi.org/10.1093/mnras/249.3.498.
20. Metcalfe, N.; Shanks, T.; Fong, R.; Roche, N. Galaxy number counts - III. Deep CCD observations to B=27.5 mag. *MNRAS* **1995**, *273*, 257–276. https://doi.org/10.1093/mnras/273.2.257.
21. Metcalfe, N.; Shanks, T.; Campos, A.; McCracken, H.J.; Fong, R. Galaxy number counts - V. Ultradeep counts: the Herschel and Hubble Deep Fields. *Monthly Notices of the Royal Astronomical Society* **2001**, *323*, 795–830. https://doi.org/10.1046/j.1365-8711.2001.04168.x.
22. McCracken, H.J.; Metcalfe, N.; Shanks, T.; Campos, A.; Gardner, J.P.; Fong, R. Galaxy number counts - IV. Surveying the Herschel Deep Field in the near-infrared. *Monthly Notices of the Royal Astronomical Society* **2000**, *311*, 707–718. https://doi.org/10.1046/j.1365-8711.2000.03096.x.
23. Durham Galaxy Number-Counts, 2010, [https://astro.dur.ac.uk/ nm/pubhtml/counts/kdata.txt]. Accessed: 2022-02-07.
24. Gardner, J.P.; Sharples, R.M.; Frenk, C.S.; Carrasco, B.E. A Wide-Field [ITAL]K[/ITAL]-band Survey: The Luminosity Function of Galaxies. *The Astrophysical Journal* **1997**, *480*, L99–L102. https://doi.org/10.1086/310630.
25. De Propris, R.; Stanford, S.A.; Eisenhardt, P.R.; Holden, B.P.; Rosati, P. The Rest-Frame K-Band Luminosity Function of Galaxies in Clusters to z= 1.3. *The Astronomical Journal* **2007**, *133*, 2209–2215. https://doi.org/10.1086/513516.
26. Huang, J.S.; Glazebrook, K.; Cowie, L.L.; Tinney, C. The Hawaii+Anglo-Australian Observatory K-Band Galaxy Redshift Survey. I. The Local K-Band Luminosity Function. *ApJ* **2003**, *584*, 203–209, [arXiv:astro-ph/astro-ph/0209440]. https://doi.org/10.1086/345619.
27. Kochanek, C.S.; Pahre, M.A.; Falco, E.E.; Huchra, J.P.; Mader, J.; Jarrett, T.H.; Chester, T.; Cutri, R.; Schneider, S.E. The K-Band Galaxy Luminosity Function. *The Astrophysical Journal* **2001**, *560*, 566–579. https://doi.org/10.1086/322488.
28. Ellis, R.S. Faint Blue Galaxies. *ARA&A* **1997**, *35*, 389–443, [arXiv:astro-ph/astro-ph/9704019]. https://doi.org/10.1146/annurev.astro.35.1.389.
29. Windhorst, R.A.; Cohen, S.H.; Hathi, N.P.; et al. The Hubble Space Telescope Wide Field Camera 3 Early Release Science Data: Panchromatic Faint Object Counts for 0.2-2 μm Wavelength. *ApJS* **2011**, *193*, 27, [arXiv:astro-ph.CO/1005.2776]. https://doi.org/10.1088/0067-0049/193/2/27.
30. Yasuda, N.; Fukugita, M.; Narayanan, V.K.; et al. Galaxy Number Counts from the Sloan Digital Sky Survey Commissioning Data. *AJ* **2001**, *122*, 1104–1124, [arXiv:astro-ph/astro-ph/0105545]. https://doi.org/10.1086/322093.
31. Shanks, T.; Stevenson, P.R.F.; Fong, R.; MacGillivray, H.T. Galaxy number counts and cosmology. *Monthly Notices of the Royal Astronomical Society* **1984**, *206*, 767–800. https://doi.org/10.1093/mnras/206.4.767.
32. McDonald, M.; Bayliss, M.; Benson, B.A.; et al. A massive, cooling-flow-induced starburst in the core of a luminous cluster of galaxies. *Nature* **2012**, *488*, 349–352, [arXiv:astro-ph.CO/1208.2962]. https://doi.org/10.1038/nature11379.

33. Atek, H.; Richard, J.; Jauzac, M.; et al. Are ultra-faint galaxies at $z = 6 - 8$ responsible for cosmic reionization? Combined constraints from the Hubble Frontier Fields, clusters and parallels. *The Astrophysical Journal* **2015**, *814*, 69. https://doi.org/10.1088/0004-637x/814/1/69.
34. Ellis, R.S.; Colless, M.; Broadhurst, T.; Heyl, J.; Glazebrook, K. Autofib Redshift Survey - I. Evolution of the galaxy luminosity function. *MNRAS* **1996**, *280*, 235–251. https://doi.org/10.1093/mnras/280.1.235.
35. Cohen, J.G. A Progress Report on the Caltech Faint Galaxy Redshift Survey. In Proceedings of the Deep Fields; Cristiani, S.; Renzini, A.; Williams, R.E., Eds., 2001, p. 49, [arXiv:astro-ph/astro-ph/0012004]. https://doi.org/10.1007/10854354_10.
36. Arnouts, S.; Schiminovich, D.; Ilbert, O.; et al. The GALEX VIMOS-VLT Deep Survey Measurement of the Evolution of the 1500 Å Luminosity Function. *ApJL* **2005**, *619*, L43–L46, [arXiv:astro-ph/astro-ph/0411391]. https://doi.org/10.1086/426733.
37. Kuhn, L.; Shubat, M.; Barmby, P. Comparing NED and SIMBAD classifications across the contents of nearby galaxies. *MNRAS* **2022**, *515*, 807–816, [arXiv:astro-ph.IM/2206.13311]. https://doi.org/10.1093/mnras/stac1801.
38. Blanton, M.R.; Lupton, R.H.; Schlegel, D.J.; Strauss, M.A.; Brinkmann, J.; Fukugita, M.; Loveday, J. The Properties and Luminosity Function of Extremely Low Luminosity Galaxies. *ApJ* **2005**, *631*, 208–230, [arXiv:astro-ph/astro-ph/0410164]. https://doi.org/10.1086/431416.
39. Padovani, P. The microjansky and nanojansky radio sky: source population and multiwavelength properties. *MNRAS* **2011**, *411*, 1547–1561, [arXiv:astro-ph.CO/1009.6116]. https://doi.org/10.1111/j.1365-2966.2010.17789.x.
40. Kellermann, K.I.; Condon, J.J.; Kimball, A.E.; Perley, R.A.; Ivezić, Ž. Radio-loud and Radio-quiet QSOs. *ApJ* **2016**, *831*, 168, [arXiv:astro-ph.GA/1608.04586]. https://doi.org/10.3847/0004-637X/831/2/168.
41. Radcliffe, J.F.; Barthel, P.D.; Garrett, M.A.; Beswick, R.J.; Thomson, A.P.; Muxlow, T.W.B. The radio emission from active galactic nuclei. *A&Ap* **2021**, *649*, L9, [arXiv:astro-ph.GA/2104.04519]. https://doi.org/10.1051/0004-6361/202140791.
42. Griffiths, R.E.; Ratnatunga, K.U.; Casertano, S.; et al. The HST Medium Deep Survey: progress towards resolution of the faint blue galaxy problem. *Astrophysical Letters and Communications* **1997**, *36*, 355–361.
43. Schneider, P. *Extragalactic astronomy and cosmology: An introduction*; Springer Berlin, Heidelberg, 2006; pp. 1–459. https://doi.org/10.1007/978-3-540-33175-9.
44. Windhorst, R.A. The microJansky and nanoJansky population. *New Astron. Rev.* **2003**, *47*, 357–365. https://doi.org/10.1016/S1387-6473(03)00045-9.
45. Owen, E.R.; Wu, K.; Jin, X.; Surajbali, P.; Kataoka, N. Starburst and post-starburst high-redshift protogalaxies. The feedback impact of high energy cosmic rays. *A&Ap* **2019**, *626*, A85, [arXiv:astro-ph.GA/1905.00338]. https://doi.org/10.1051/0004-6361/201834350.
46. Ellis, R.S. *Unsolved Problems in Astrophysics*; Princeton Univ. Press: Princeton, 1996.
47. Driver, S.P.; Fernández-Soto, A.; Couch, W.J.; et al. Morphological Number Counts and Redshift Distributions to I<26 from the Hubble Deep Field: Implications for the Evolution of Ellipticals, Spirals, and Irregulars. *ApJL* **1998**, *496*, L93–L96, [arXiv:astro-ph/astro-ph/9802092]. https://doi.org/10.1086/311257.
48. Edwards, L.O.V.; Salinas, M.; Stanley, S.; et al. Clocking the formation of today's largest galaxies: wide field integral spectroscopy of brightest cluster galaxies and their surroundings. *MNRAS* **2020**, *491*, 2617–2638, [arXiv:astro-ph.GA/1909.10434]. https://doi.org/10.1093/mnras/stz2706.
49. Tyson, J.A. Deep CCD Survey: Galaxy Luminosity and Color Evolution. *AJ* **1988**, *96*, 1. https://doi.org/10.1086/114786.
50. Wyithe, J.S.B.; Oh, S.P.; Pindor, B. A possible gravitational lensing explanation for the excess of strong Mg ii absorbers in gamma-ray burst afterglow spectra. *Monthly Notices of the Royal Astronomical Society* **2011**, *414*, 209–217. https://doi.org/10.1111/j.1365-2966.2011.18374.x.